J. Fluid Mech. (1998), *vol.* 376, *pp.* 61–90. Printed in the United Kingdom

Examination of the flow near the leading edge of attached cavitation. Part 1. Detachment of two-dimensional and axisymmetric cavities

By A. TASSIN LEGER AND S. L. CECCIO

Department of Mechanical Engineering and Applied Mechanics, University of Michigan, Ann Arbor, MI 48109-2121, USA

(Received 21 August 1997 and in revised form 11 May 1998)

The flow near the cavity detachment region of stable attached cavitation was examined using qualitative and quantitative flow visualization. The non-cavitating and cavitating flows around a hydrophilic brass and hydrophobic Teflon sphere and cylinder were examined. The location of non-cavitating boundary layer separation and cavity detachment was related to the free-stream Reynolds and cavitation numbers. The shape of the cavity near the detachment was greatly affected by the material of the cavitating object. The cavity interface on the hydrophilic test objects curved downstream to form a forward facing step. A region of recirculating fluid existed upstream of the cavity interface. The cavity detachment on the hydrophobic test objects was much closer to the location of boundary layer separation. The forward facing step and the recirculating region were nearly absent.

The measured flow field near the surface of the brass sphere, cylinder, and hydrofoils under cavitating and non-cavitating conditions was used to calculate the position of two-dimensional laminar boundary layer separation. Thwaites' and Stratford's methods were used to predict the location of boundary layer separation upstream of the cavity detachment. The predictions compared well with the observed position of separation.

1. Introduction

Sheet or attached cavitation can form on the lift-producing surfaces of turbomachinery and propellers. Such cavitation occurs when the flowing liquid separates from the solid surface resulting in a relatively stable vapour film. If the liquid/vapour interface re-closes on the solid surface of the cavitating object, the flow is termed 'partial cavitation' while the cavity of a 'supercavitating flow' re-closes downstream of the cavitating object. Partial cavitation can be further classified as either 'closed' ('stable') or 'open' ('unstable') attached cavitation depending on the flow in the closure region of the cavity. A closed partial cavity has a relatively stable cavity length, while an open cavity has a periodically varying length which is associated with the shedding of large clouds of bubbles. Cavities formed almost entirely of vapour are called 'natural' cavities, and gas is injected into a 'ventilated' cavity.

Researchers have examined attached cavitation in order to predict cavity inception and the final cavity geometry. Many models of attached cavitation employ a criterion whereby attached cavitation forms when the pressure near the surface falls below

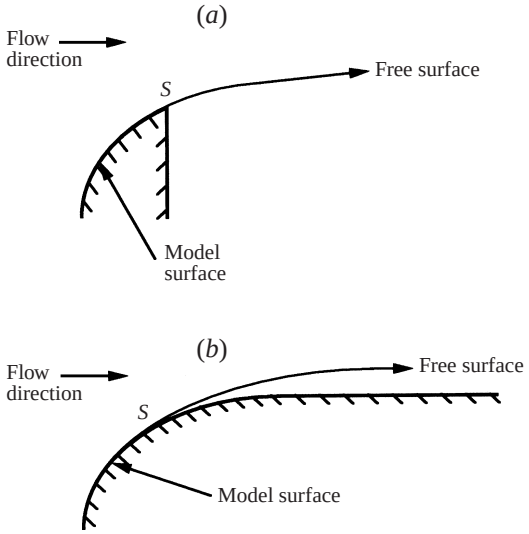

FIGURE 1. Schematic diagram of (*a*) fixed and (*b*) free detachment of a two-dimensional cavity.

vapour pressure ($C_{p,min} = -\sigma$). The stable location of the developed cavity detachment is usually determined *a priori* after employing empirical criteria. Efforts to improve the modelling of attached cavitation should begin with an examination of the cavity detachment from smooth surfaces.

Attached cavities are often modeled using the assumption of potential flow. A free streamsurface is used to represent the cavity/liquid interface. Two-dimensional cavities are modelled with a streamline. The streamline can either detach from an abrupt detachment point (such as a vertex or a surface discontinuity) or it can detach smoothly from the wetted surface (figure 1). The location of cavity detachment in the former case is well defined (fixed), while the detachment point on the smooth surface is not necessarily known in advance (free). In considering a two-dimensional potential flow model of the cavity detachment, we can examine the complex velocity, $w = u - \mathrm{i}v$, at the point of cavity detachment, S. It is useful to employ the Hodograph transformation, $\omega(z)$:

$$\omega(z) = \ln\frac{q_c}{|w|} + \mathrm{i}\tan^{-1}\frac{v}{u} \tag{1.1}$$

where q_c is the (constant) flow speed on the cavity surface and $z = r\mathrm{e}^{\mathrm{i}\theta}$ using polar coordinates with the origin at the point of cavity detachment. Near the origin, $\mathrm{Re}[\omega(z)] = 0$ on the free surface ($\theta = 0$) and $\mathrm{Im}[\omega(z)] = 0$ on the solid surface ($\theta = \pi$). Thus, to first order, $\omega(z)$ near a fixed detachment is given by

$$\omega(z) = C\mathrm{i}z^{1/2} + \cdots \tag{1.2}$$

where C is a flow specific constant. This formulation results in unrealistic predictions about the flow such as infinite flow acceleration toward the detachment point along the wetted surface and infinite curvature of the free surface at the point of cavity detachment. For the case of a free detachment, the location of the detachment point is unknown, so the position may be chosen such that the constant C is identically zero. In this case, $\omega(z)$ near detachment is given by

$$\omega(z) = \hat{C}\mathrm{i}z^{3/2} + \cdots \tag{1.3}$$

where $\hat{C}$ is a new flow specific constant. After the appropriate choice of detachment location, the velocity and pressure gradients at the point of cavity detachment tend toward zero as the cavity detachment point is approached, and the cavity and free surface curvature are equal at the point of cavity detachment (Brennen 1995). This is the 'smooth detachment' or the Brillouin–Villat condition for cavity detachment from smooth surfaces (Brillouin 1911; Villat 1914).

Experimental examination of free cavity detachment has shown that the smooth detachment condition rarely exists. Brennen (1969*b*) numerically simulated the potential cavity flow around bluff bodies after employing the Brillouin–Villat condition for cavity detachment. His predicted location of cavity detachment was substantially upstream of the experimentally observed location. It was observed that the cavity does not undergo a smooth detachment (i.e. the cavity and solid surface do not have equal curvature at the detachment point). Brennen suggested that viscous effects were principally responsible for these differences.

The role of viscosity during smooth cavity separation was examined experimentally by Arakeri & Acosta (1973, 1976) and Arakeri (1975) for bluff body cavitation. Schlieren imaging of the cavity detachment region revealed that laminar boundary layer separation existed upstream of the cavity detachment point. Moreover, elimination of the laminar boundary layer separation (through artificial stimulation of the boundary layer to turbulence) could in some cases prevent a stable attached cavity from forming. The cavity detachment did not satisfy the smooth detachment criterion and the location of the cavity separation point was not necessarily near the location of non-cavitating boundary layer detachment. The location of boundary layer separation was a strong function of cavitation number and a weak function of the Reynolds number. Figure 2 shows a schematic diagram of the cavity detachment region as proposed by Arakeri (1975). Arakeri offered correlations to predict the location of laminar boundary layer separation upstream of the cavity as well as the distance between the position of boundary layer separation and the cavity detachment, λ. The detailed flow near the cavity detachment from the surface was related to viscous and surface tension forces through use of the Taylor–Saffman number, $\mu U_o/\lambda_{lg}$, where μ is the liquid dynamic viscosity, U_o is the free-stream velocity, and γ_{lg} is the liquid/gas interfacial tension.

Franc & Michel (1985) examined the flow over a series of bodies, including hydrofoils. They also recognized the relationship between the presence of non-cavitating boundary layer separation and the formation of attached cavitation. Their results confirmed the inadequacies of the Brillouin–Villat condition and illustrated some limitations of Arakeri's correlations. They proposed a new cavity detachment criterion based on the interaction of the cavity flow with the boundary layer upstream of the cavity detachment. Figure 3 presents a schematic interpretation of the steps necessary to form a stable attached cavity. An incipient cavity will form in the region of non-cavitating laminar boundary layer separation. The presence of the cavity alters the entire flow field, including the viscous boundary layer upstream of the incipient cavity. As the cavitation number is lowered, the developed cavity detachment region will move until it coincides with the new point of laminar boundary separation upstream of the cavity (if a stable cavity occurs).

Franc & Michel (1985) posed the 'cavity detachment paradox.' A cavity must be preceded by laminar boundary layer separation. However, the pressure within a natural cavity is very close to the vapour pressure of the cavitating liquid. If the cavity pressure is the lowest pressure in the flow, there would be a favourable pressure gradient upstream of the cavity and laminar separation would not be expected. Must

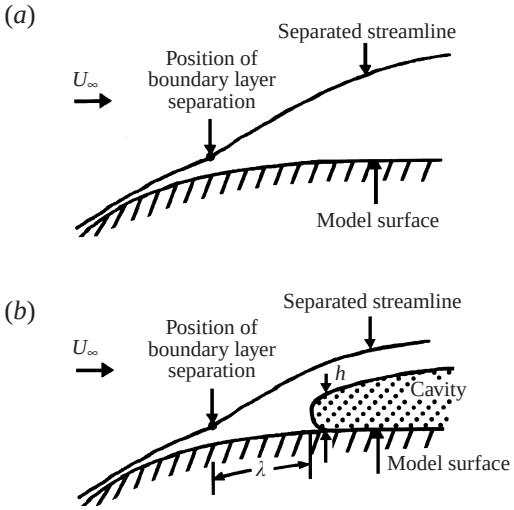

FIGURE 2. Schematic diagram of the cavity detachment region proposed by Arakeri (1975).

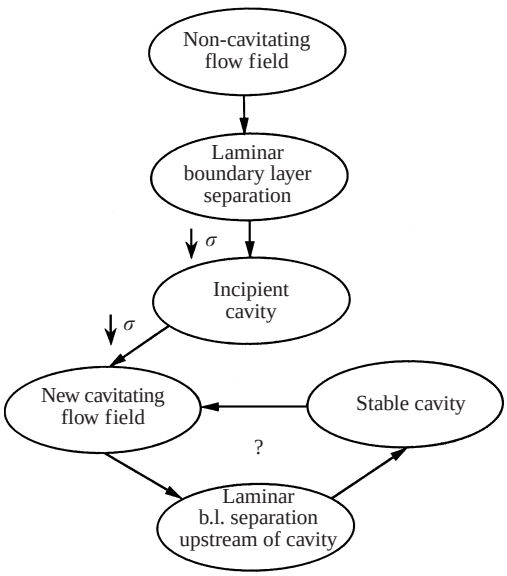

FIGURE 3. A diagram showing the steps necessary to form a stable attached cavity.

the fluid upstream of the cavity be in tension (or have a lower pressure than the cavity pressure, in the case of a ventilated cavity)? Considering two-dimensional or axisymmetric cavities, the laminar separation streamlines and the cavity free streamline enclose a region of fluid bounded by two stagnation points. This would suggest that there is a fluid sink downstream of the cavity without a corresponding source in the flow. Need the flow recirculate upstream of the cavity, or must the flow be three-dimensional?

In the present work, the flow near the cavity detachment region will be examined and unresolved issues raised above will be explored. Qualitative and quantitative flow visualization will be employed to examine the flow near the detachment region of nominally two-dimensional cavities. The interaction of the viscous flow upstream of

the cavity with the cavity itself is examined along with the influence of interfacial tension. Measurements of the flow field will be used to analyse the predictive methods proposed by Franc & Michel and the 'cavity paradox' will be addressed.

2. Experimental methods

Several techniques were employed for qualitative and quantitative flow analysis: dye injection, streak visualization, high speed video imaging, and planar particle image velocimetry (PIV). These techniques are described below, along with a description of the blow-down water tunnel and the test objects.

2.1. *Blow-down water tunnel*

The present study employed the blow-down water tunnel (BDWT) of the Cavitation and Multiphase Flow Laboratory at the University of Michigan. It consists of two 1500 l tanks both connected to vacuum pumps and an air compressor. A square contraction, of area ratio 4.4:1, connects the upper tank to the test section. The test section has a 76.2 mm square cross-section that is approximately 260 mm long. Water is drawn into the upper tank, de-aerated, and then forced through the test section and into the lower tank. The tunnel can operate with a maximum velocity of 20 m s^{-1}, and the test section pressure can range from vacuum to 690 kPa. The amount of steady flow which can be achieved depends on the steady velocity of the tunnel. At the fastest speed, approximately 6 s of steady flow can be achieved. The initial starting pressure of a blow-down can be set independently of the velocity of the fluid, allowing the study of both cavitating and non-cavitating flows at the same speed. The entire process is controlled by a custom designed computer program. The test section is accessed by four removable windows made completely of polycarbonate or of aluminium with a 75 mm diameter optical flat flush-mounted to the flow surface. In general, the optical flat permits laser beam access while the polycarbonate window permits complete visual/photographic access. The objects of study can either be mounted on a support or directly on the windows of the test section, depending on the shape and size of the object. An advantage of the BDWT is the experimenter's ability to influence the free-stream nuclei content of the flow. By allowing the water to settle before the blow down, the free-stream nuclei will rise to the two free surfaces of the water. In this way, almost all the active nuclei can be removed from the free stream. Also, by choosing the amount of time the water settles, the experimenter can roughly control the free-stream turbulence level.

Two pressure transducers are used to measure the absolute test section pressure and the differential pressure between the test section and the upper tank. The differential pressure has been calibrated to determine the average velocity in the test section. The calibration procedure involved first scaling the output of the pressure transducer with the differential pressure measured with a mercury manometer. Then, the velocity was determined using the steady form of Bernoulli's equation. This calculated velocity was compared for the full range of flow speeds in the BDWT with measurements from a Dantec Model 55X one-component laser Doppler velocimetry (LDV) system with the probe volume positioned in the centre of the test section. The velocity from the pressure transducer matched the LDV velocity within the experimental error of both devices. It should be noted that since the steady form of the Bernoulli equation was used to calculate the velocity from the differential pressure, the calculated velocity during the beginning of a blow-down is not accurate. For the experiments presented

here, only the steady-speed portion of each blow-down was employed during data collection.

2.2. *Test objects*

Six different objects were employed during these experiments: a 25.4 mm diameter brass sphere, a 25.4 mm diameter Teflon sphere, a 19.0 mm diameter brass circular cylinder, a 19.0 mm diameter Teflon circular cylinder, a NACA 63_1A012 brass hydrofoil with a 82.8 mm chord and 9.9 mm maximum thickness, and a custom-designed brass hydrofoil with a chord of 114 mm and a 10 mm maximum thickness. The cylinder and sphere were chosen as test objects because the non-cavitating and cavitating flow field around them has been studied by many other researchers, thus allowing comparison with previous experiments. The sphere and cylinder also have very steep pressure gradients near the region of cavity detachment compared with the shallow pressure gradients near the cavity detachment on the hydrofoils.

The 25.4 mm diameter brass sphere was mounted on a support within the BDWT test section. The surface of the sphere was highly polished to an average roughness of less than 0.1 μm. The support was plumbed to permit injection of air into the cavity and also injection of dye on the surface of the sphere. Five 203 μm diameter holes were placed in the sphere at an angular location of 22.5° measured from the stagnation point. Fluorescein dye was injected through these holes to permit visualization of the flow near the surface of the sphere. The five dye holes were spaced 22.5° azimuthally apart, thus falling within one quarter of the sphere circumference. By examining the three-quarters of the sphere circumference without holes, it was determined that the dye holes did not alter the local flow around the sphere. The Teflon sphere was similar to the brass sphere, but was not instrumented with holes for dye injection. It was mounted on the same support as the brass sphere and the surface was polished smooth with a average surface roughness on the order of 1 μm. The test section area blockage of the spheres was 8.7%.

The cylinder was mounted on one of the aluminium test section windows. The surface of the cylinder was highly polished to an average roughness of less than 0.1 μm. Air was injected into the rear of the cylinder through the aluminium window and dye was introduced onto the surface of the cylinder from the opposite polycarbonate test section window. A single 203 μm diameter dye hole was placed 22.5° along the circumference of the cylinder measured from the stagnation point. Due to the large wake/cavitation area behind the cylinder, it was possible to inject air into the cavitation pocket easily and to measure the actual pressure behind the cylinder. A tube was inserted through the test section window into the wake region to measure the difference between the cavity pressure and the upstream test section pressure. The cavity behind the cylinder always extended past the location of the pressure measuring tube and generally extended past the bottom of the test section windows. The 19.0 mm diameter Teflon cylinder was actually a smooth Teflon sleeve (average surface roughness on the order of 1 μm) mounted on a brass cylindrical core, to provide a rigid mounting on the test section window. The Teflon cylinder had air injection ports, but no dye injection holes. The test section area blockage of the cylinders was 25%.

Air was injected into the wake of the sphere and cylinder to form a fully developed cavity. The cavity pressure was measured using a tube inserted through the test section window and positioned directly under the sphere within the cavitating wake. This tube was connected to a Setra model 228-1 differential pressure transducer to measure the difference between the cavity pressure and the upstream test section pressure.

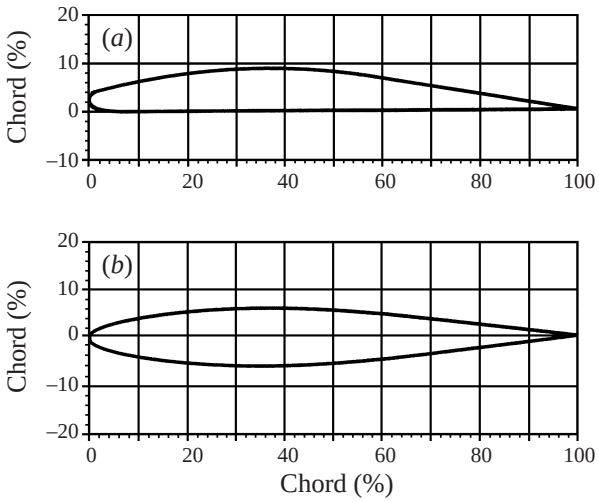

FIGURE 4. Cross-sections of the two-dimensional hydrofoils employed in the present study. (*a*) A custom-designed hydrofoil with maximum thickness of 10 mm and chord of 114 mm occurring at 36% of the chord measured from the leading edge. (*b*) A NACA 63_1A012 hydrofoil with a maximum thickness of 9.9 mm located at 35% of the chord with a chord length of 82.9 mm.

Two rectangular planform hydrofoils were used in the study. The first was a (symmetrical) NACA 63_1A012 hydrofoil which has been previously studied in detail by Li & Ceccio (1996). The maximum thickness of the hydrofoil was 9.9 mm with a chord length of 82.9 mm. The maximum thickness point was located at 35% of the chord length as measured from the leading edge. The shape of the hydrofoil cross-section is shown in figure 4(*a*). The second hydrofoil shape was custom-designed to permit holography through the glass hydrofoil (which is discussed in Part 2, Tassin Leger, Ceccio & Bernal 1998). A brass hydrofoil of the same custom shape was fabricated. Figure 4(*b*) shows the shape of this custom hydrofoil. The chord of the hydrofoil was approximately 114 mm long with a maximum thickness of 10 mm. The maximum thickness occurs at 36% of the chord. The hydrofoil was designed around a central cylindrical lens shape. The focal length of the cylindrical lens in air was 300 mm; in the water in the test section, the effective focal length was approximately 908 mm. The lens shape permits a known distortion to the holographic recording system, which can be optically corrected for by a matching cylindrical lens outside the test section. The leading edge of the hydrofoil shape was designed such that there would be no leading-edge cavitation and no cavitation on the pressure side of the hydrofoil to block optical access. The only cavitation desired was mid-chord cavitation. The hydrofoil shape was designed with the aid of a panel method to calculate the coefficient of pressure around the entire surface of the hydrofoil. Once a reasonable shape was found, a foil was fabricated and tested in the BDWT. An attack angle, α, was chosen such that the desired cavitation patterns occurred. Angles $\alpha = 1.5^\circ$ and 3.0° were chosen for study. These angles were measured between the flat surface of the hydrofoil and the free-stream flow direction. The true attack angle is 1.5° greater. Both the glass and the brass hydrofoils were polished to a surface roughness of less than 0.1 μm.

The brass hydrofoils were mounted on one aluminium test section. The side of the brass hydrofoils opposite from the mounting window was rounded off to prevent edge cavitation from blocking the side view of the hydrofoil. There was no air injection

on the hydrofoils and the cavities consisted almost completely of water vapour. The pressure inside the cavity was not measured, but assumed to be the vapour pressure of water at room temperature. The area blockage due to the NACA hydrofoil was 13%. The custom hydrofoil blocked the test section by 15% for $\alpha = 1.5^\circ$ and 18% for $\alpha = 3.0^\circ$.

2.3. *Flow visualization*

Fluorescein dye injection on the surface of the brass sphere and brass cylinder was used to visualize the flow field in the boundary layer of the liquid and over the surface of the attached cavitation and to locate the positon of laminar boundary layer separation. From a side view of one dye stream, quantitative information on the flow separation and cavitation attachment points can be determined. Either a Strobolume strobe light or a Model 95 Lexel Argon-Ion laser (1 W maximum power at 488 nm wavelength) was used to illuminate the dye and make it fluoresce green, and the image was recorded using a 35 mm Nikon camera. A trigger was used to simultaneously record the test conditions at the time of the photograph. During most of the run conditions in the BDWT, the static test section pressure was such that dye was sucked into the boundary layer. At high static pressures and high velocities, however, it was usually necessary to pump the dye into the flow using a large syringe. The force that could be applied to the syringe was the limiting factor on the dye injection technique. This limit was reached rather early for non-cavitating, high speed flows.

Streak visualization was used to visualize the streamlines in the flow near the region of cavity detachment. It was also used to determine the location of flow separation and cavity detachment on objects without dye injection holes. A schematic diagram of the set-up is shown in figure 5(*a*). A Model 95 Lexel Argon-Ion laser (1.5 W maximum power, 514 nm) was used to illuminate a plane of the flow perpendicular to the test object. A 35 mm Nikon camera was positioned perpendicular to the light sheet to record the seeded flow through the laser light. The flow was seeded with either 12 μm hollow glass spheres or with 20–40 μm fluorescing polymer spheres. It was necessary to have a low seeding density, since too many particles would blur out individual streaks. The red-fluorescing polymer spheres were required when the background scattering from the laser was too strong and obscured the streaks of the glass spheres. A filter on the camera lens blocked out the 514 nm wavelength of the laser but permitted the red fluorescence to pass. The fluorescing particles were used during the experiments on the Teflon objects, since the white surface of the Teflon scattered excessive light into the background. Streak visualization was used to measure the flow separation and the cavity detachment locations on the Teflon objects as well as on the brass hydrofoils. Both dye visualization and streak visualization were used on the brass sphere to test the validity of finding the flow separation and cavity detachment using streak visualization. The streak visualization and the dye visualization yielded results of similar accuracy (± 0.5 mm).

Double-pulsed planar particle imaging velocimetry (PIV) was used to determine the velocity field in a plane perpendicular to the attached cavity. The set-up used is similar to that employed during the study of bubble cavitation by Tassin *et al.* (1995), and a schematic diagram is shown in figure 5(*b*). A plane of light was positioned perpendicular to the surface of the hydrofoil, and parallel to the direction of the free-stream flow. Two frequency-doubled Quanta Ray GCR 130-30 Nd-YAG lasers were used to produce the double-pulsed light sheet. These lasers have a design repetition rate of 30 Hz with a maximum energy of 100 mJ in a 7 ns pulse. Since the light sheet

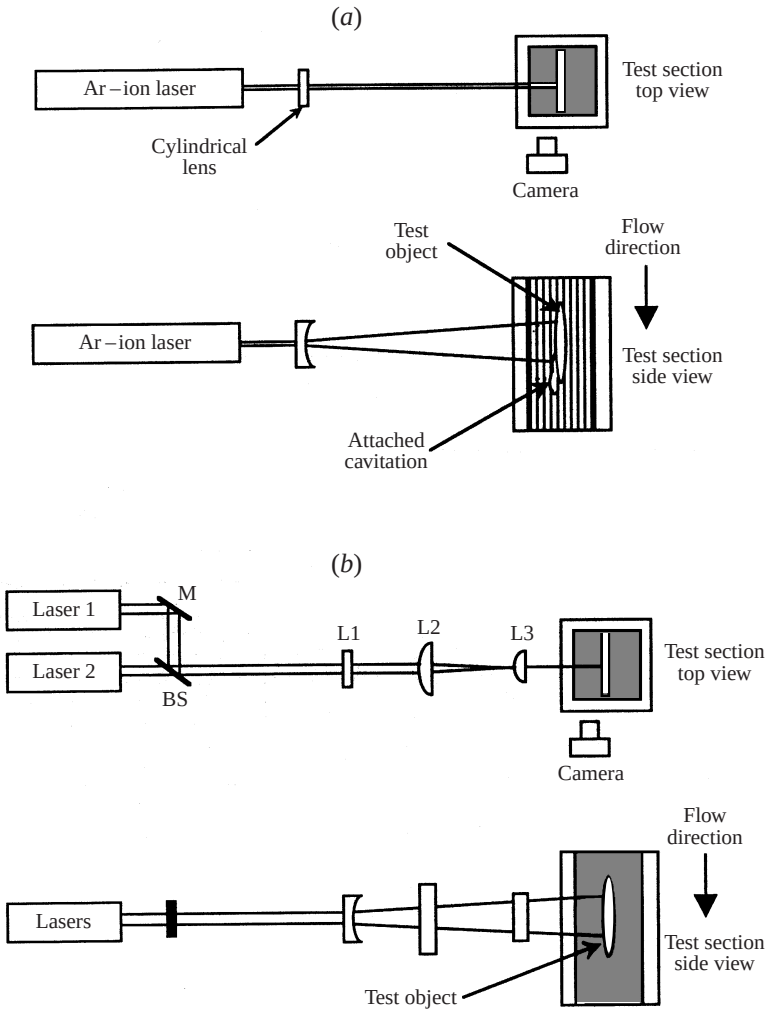

FIGURE 5. (*a*) A schematic diagram showing the set-up for streak visualization. Streak visualization was used to determine the streamlines in the flow near the region of cavity detachment and the location of flow separation and cavity detachment on objects without dye injection holes. (*b*) A schematic diagram showing the setup for double-pulsed planar particle imaging velocimetry (PIV). PIV was used to determine the velocity field in a plane perpendicular to the attached cavity. A plane of light was positioned perpendicular to the surface of the hydrofoil, and parallel to the direction of the free-stream flow.

was produced from the light of two separate lasers, the time between the light sheets could be greatly varied. Light was then scattered by seed particles in the fluid and captured on film with a 35 mm Nikon camera positioned perpendicular to the light sheet. The particles were hollow glass spheres with silvered surfaces and were 12 μm in diamter. The magnification of the camera could be adjusted to suit the necessary field of view using any combination of a Micro-Nikkor 105 mm lens, bellows, and 2× converters. The time between exposures was measured for each image by recording the Q-switch synchronization signals of the lasers using a Hewlett Packard 54620A 16 Channel 500 Megasamples/second Logic Analyzer. The time interval was known to within 50 ns. The typical pulse separation time was 10 μs.

FIGURE 6. A side view of the cavity detachment region with associated dye visualization on the brass sphere. The surface of the cavity forms a sharp curve as it detaches from the solid surface indicating a hydrophilic surface.

The processing of the PIV images was conducted in several steps. First, the pictures were scanned at 2700 d.p.i. using a Nikon Coolscan negative scanner. For the sphere and cylinder, the magnification of the image was determined after examining the arc of the surface captured in the image. For the hydrofoils, the light sheet did not cover the entire negative. The magnification was determined by measuring the size of the light sheet in the test section and comparing it to the size on the negative. After the magnification was determined, the test object in the digitized image was manually outlined and painted black to remove any random bright spots that might be mistaken as particle-pairs. The final step of the PIV analysis used a program called Visiflow (AEA Technology, distributed by Oxford Lasers) to perform numerical autocorrelation on the scanned negative images. The autocorrelation was performed within a box of 256 by 256 pixels. The boxes were overlapped by 75% to get closely spaced vectors without having to perform a post-autocorrelation interpolation. The autocorrelation routine attained sub-pixel accuracy on the location of the correlation peak by using a Gaussian optimization routine to find the correlation peak. The majority of particle pairs were separated by fourteen or more pixels, which gives a conservative ± 1 pixel error of $\pm 7\%$.

3. Flow near the detachment of a stable cavity

3.1. *Brass sphere and cylinder*

The flow in the vicinity of the cavity detachment was examined for ventilated cavity flows over both the sphere and cylinder. Figure 6(*a*) presents a side view of the cavity detachment region with associated dye visualization on the brass sphere. The surface of the cavity forms a sharp curve as it detaches from the solid surface indicating a hydrophilic surface. Figure 7 shows a similar flow visualized with particle streaks. These time exposed images reveal slowly moving particles recirculating in the

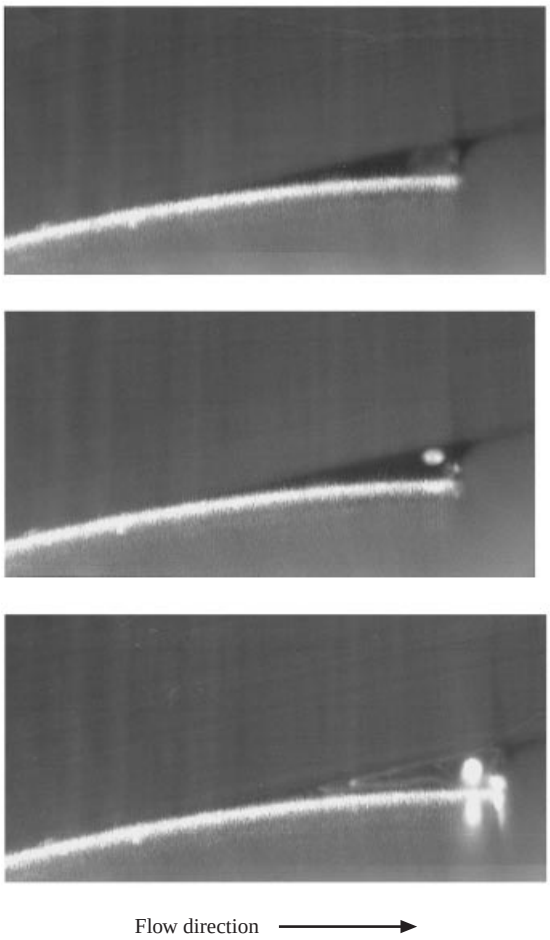

FIGURE 7. Side views of the cavity detachment region with particle streak flow visualization. These time exposed images reveal slowly moving particles recirculating in the separation region bounded by the cavity interface and the separation streamline.

separation region bounded by the cavity interface and the separation streamline. The flow patterns observed here are similar to those recorded by Arakeri (1975) using schlieren flow visualization.

The cavity has a finite thickness near the point of detachment which forms a forward facing step. The 'step height', h, is defined in figure 2 and is approximately twice the radius of curvature of the cavity leading edge. h was measured from photographs with an uncertainty of ± 25 μm. The step height is a function of both the Reynolds number and cavitation number. Interfacial tension between the liquid and cavity gas will result in a pressure difference across the interface in this region of steep curvature. The pressure jump across the cavity at the point of detachment, $P_d - P_c$, is approximated by $\gamma_{lg}/\frac{1}{2}h$ where P_d is the pressure on the liquid side of the cavity interface, and γ_{lg} is the liquid/gas surface tension. Here, $P_d - P_c/\frac{1}{2}\rho U_o{}^2 = 4\gamma_{lg}/h\rho U_o{}^2 \approx 0.01$. The local cavitation number in the liquid near cavity detachment is only slightly modified. Thus, it is expected that the gas/liquid interfacial tension will not play a significant role in the process of cavity detachment, as was suggested by Brennen (1970), who examined the effect of surfactants on cavity flows. The cavity profile observed on

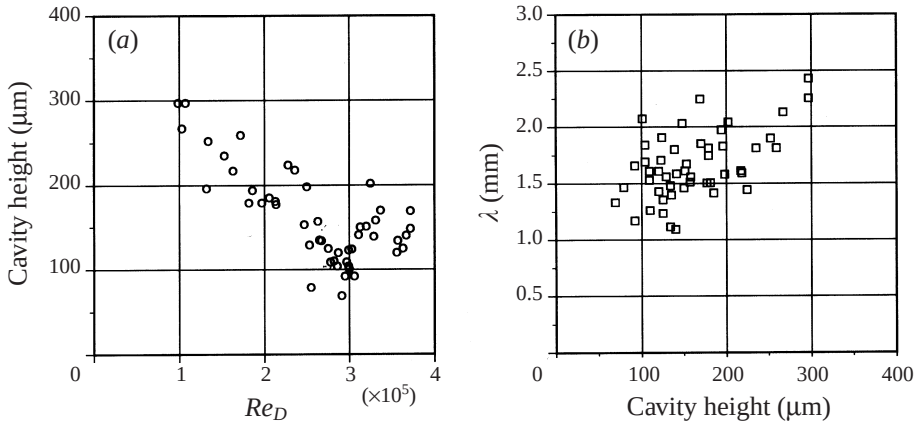

FIGURE 8. (*a*) Cavity height h as a function of Reynolds number for the cavities forming on the sphere over a range of cavitation numbers. Here, $Re_D = U_o D/\nu$, where D is the diameter of the sphere. (*b*) Distance between boundary layer separation and cavity detachment, λ as a function of cavity height, h.

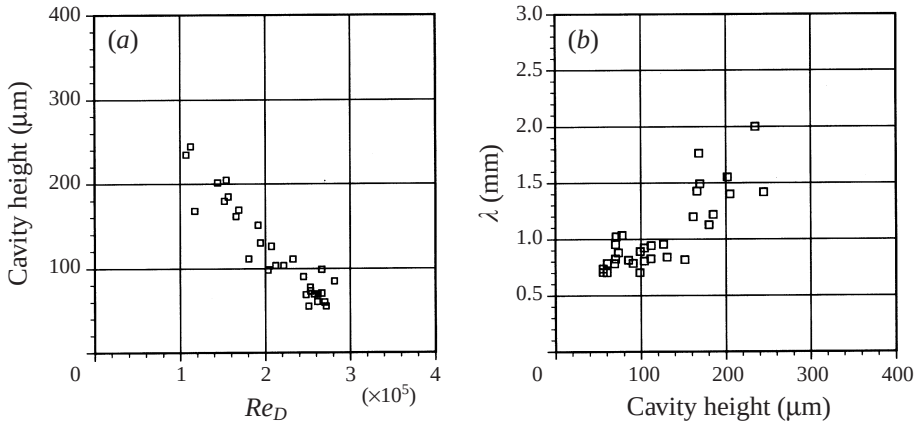

FIGURE 9. As figure 8 but for the cylinder.

the cylinder is similar in shape to the brass sphere, with a steep curvature near the detachment point.

Figure 8(*a*) presents a plot of the cavity height h as a function of Reynolds number for the cavities forming on the sphere over a range of cavitation numbers. Here, $Re_D = U_o D/\nu$, where D is the diameter of the sphere or cylinder and ν is the liquid kinematic viscosity. Figure 8(*b*) presents a plot of the distance between boundary layer separation and cavity detachment, λ, as a function of cavity height, h. Figures 9(*a*) and 9(*b*) present similar plots for cavity flows on the cylinder. The cavity step height decreases with increasing Reynolds number, and λ increases with increasing h. As the Reynolds number increases, the cavity height decreases. And, as the cavitation number is reduced, the cavity height increases. Arakeri (1975) suggested that the momentum thickness of the boundary layer just upstream of cavity detachment strongly influences the region of cavity detachment. The cavity height is dependent on the Reynolds number, but the dependence is approximately linear, while the momentum thickness will vary as $Re^{-1/2}$ for laminar boundary layers upstream of

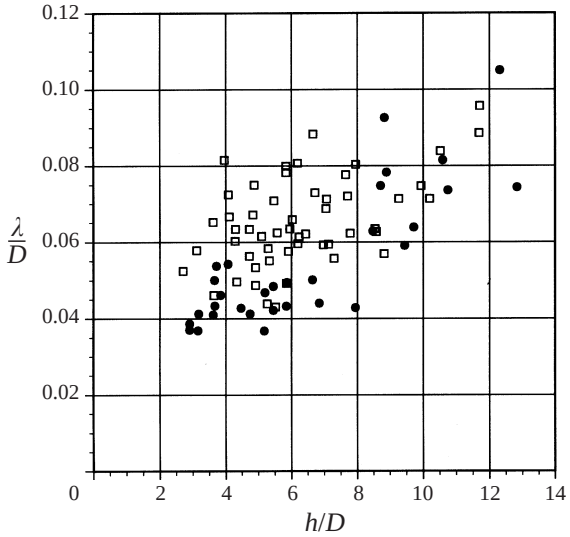

FIGURE 10. λ/D plotted against h/D for both the sphere (□) and cylinder (●).

the cavity. The distance between boundary layer separation and cavity detachment, λ, increases as h increases. Figure 10 presents λ/D plotted against h/D for both the sphere and cylinder data.

3.2. *Teflon sphere and cylinder*

By changing the material of the sphere from brass, which is hydrophilic, to Teflon, which is hydrophobic, the surface energy of the solid/liquid and solid/gas interfaces is changed significantly. For hydrophilic objects, the work of adhesion between the liquid and the solid is strong, and for hydrophobic objects, the adhesion is weak. A static contact angle can be defined at the junction of a solid, liquid, and gas and is measured from the solid through the liquid to the gas. The contact angle and the liquid interfacial tension are related to the 'work of adhesion' between the liquid and the solid, W_A:

$$W_A = \gamma_{lg}(1 + \cos\phi) \tag{3.1}$$

where γ_{lg} is the liquid/gas interfacial tension (which is appoximately equal to the liquid interfacial tension), and ϕ is the static contact angle (Davies & Rideal 1961). The work of adhesion is the work necessary to separate the liquid from the solid over a unit area. This quantity can be compared to the 'work of cohesion', W_C, which is the work necessary to cleave a volume of liquid over a unit area:

$$W_C = 2\gamma_{lg}. \tag{3.2}$$

For strongly hydrophilic solid/liquid systems (such as brass/water), $W_C \approx W_A \approx 2\gamma_{lg}$ and ϕ tends to 0°. Alternatively, for strongly hydrophobic solid/liquid systems (such as Teflon/water), $W_A \approx 0$ and ϕ tends to 180°. The difference between the work of cohesion and the work of adhesion, ΔW, is indicative of the potential surface energy of the solid/liquid interface:

$$\Delta W = W_C - W_A = \gamma_{lg}(1 - \cos\phi). \tag{3.3}$$

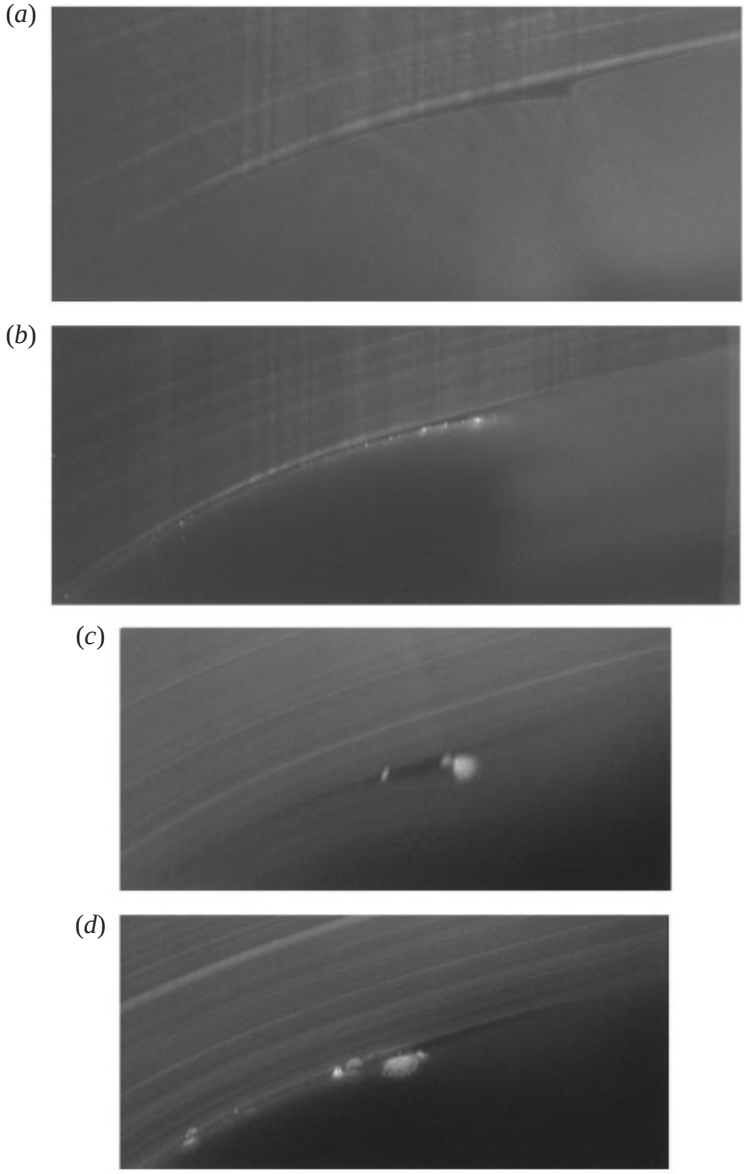

FIGURE 11. Side views of streak visualization around the edge of (*a*) the brass and (*b*) Teflon spheres and (*c*) the brass and (*d*) Teflon cylinders.

$\Delta W \approx 0$ for hydrophilic solid/liquid systems. The static contact angle for brass/water/air is near 0° while the static contact angle of the Teflon/water/air system is 108° (Davies & Rideal 1961).

Figure 11 shows two side views of streak visualization around the edge of the brass and Teflon spheres (*a, b*) and the brass and Teflon cylinders (*c, d*). The cavity interface is highly curved for the brass sphere with a contact angle of approximately 30°. For the Teflon sphere, the cavity interface is much flatter with a contact angle of approximately 150°. However, the streamlines of the liquid flow are quite similar. Figure 12 presents the relationship between λ and the free-stream Reynolds number

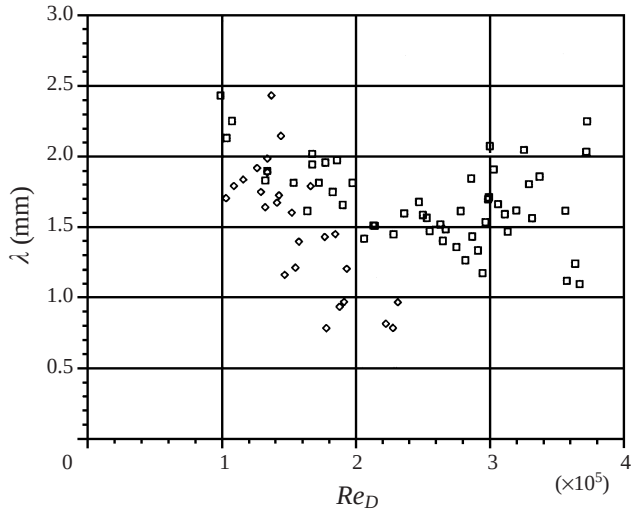

FIGURE 12. The relationship between λ and the free-stream Reynolds number for the brass (□) and Teflon (◇) spheres for a range of cavitation numbers: $0.33 < \sigma < 0.52$ for the sphere and $0.30 < \sigma < 0.63$ for the cylinder.

for the brass and Teflon spheres for a range of cavitation numbers. For the Teflon sphere the distance between the boundary layer separation and the cavity detachment became smaller as the Reynolds number increased. The region of cavity detachment on the test objects of the same material were quite similar. Bright spots on the images in figures 11(*b*) and 11(*d*) may be the result of local surface nucleation or 'hot spots' of light refected back by the cavity surface. Conventional photographs did not reveal surface nucleation on the Teflon test objects, however.

4. Boundary layer separation and cavity detachment

4.1. *Brass sphere and cylinder*

The non-cavitating flow around the brass sphere was first examined to determine whether blockage effects were significant and to determine the accuracy with which the boundary layer separation could be determined with dye injection. Figure 13 presents the angle of boundary layer separation measured from the front stagnation point as a function of Reynolds number. The data were found from side view dye visualization. Data from the present study were compared to that of Achenbach (1972) and the agreement was good. These results were also consistent with the results of Maxworthy (1969) who examined the effects of wind tunnel blockage on the pressure distribution around spheres at high Reynolds numbers. The effects of test section blockage do not appear to be significant. From the figure it can be seen that the angle of flow separation remained relatively constant at low Re_D, but sharply increased around $Re_D \sim 1.5 \times 10^5$, which was the beginning of turbulent transition in the sphere boundary layer. Once the boundary layer on the brass sphere was fully turbulent ($Re_D > 5 \times 10^6$), the angle of flow separation was again relatively constant (Achenbach 1972).

The free-stream pressure was reduced and air was injected into the wake of the brass sphere to form a fully-developed ventilated cavity. Figure 14 shows the angle of boundary layer separation and cavity detachment versus Reynolds number for a

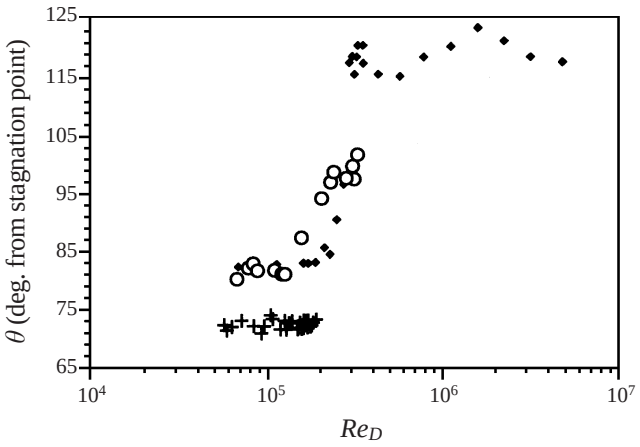

FIGURE 13. The angle of boundary layer separation measured from the front stagnation point as a function of Reynolds number for the flow over the non-cavitating sphere (○) and cylinder (+). The data of Achenbach (1972) for flow over a sphere are presented for comparison (◆)

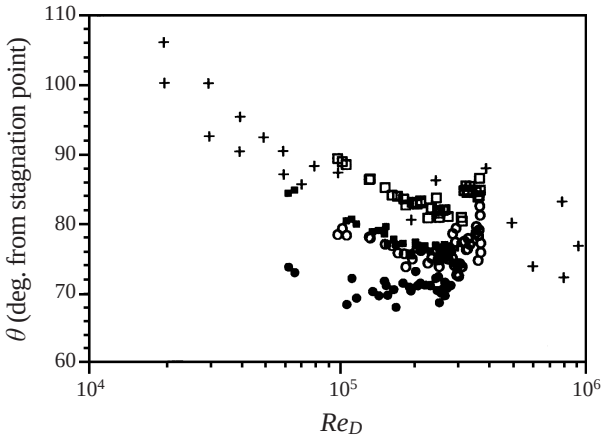

FIGURE 14. The angle of boundary layer separation (○) and cavity detachment (□) measured from the front stagnation point as a function of Reynolds number for the flow over the sphere for $\sigma = 0.3$ to 0.5 (empty symbols) and cylinder for $\sigma = 1.1$ to 1.3 (filled symbols). The data of Brennen (Arakeri 1975) for cavity detachment on a sphere are also presented for comparison for $\sigma = 0.1$ to 0.5 (+).

narrow range of cavitation numbers, $\sigma = P_o - P_c/\frac{1}{2}\rho U_o{}^2$, where P_o is the free-stream static pressure, P_c is the cavity static pressure, ρ is the fluid density, and U_o is the free-stream velocity. The cavitation numbers range from 0.33 to 0.52. Data collected by Brennen and reported by Arakeri (1975) are also shown for cavitation on 6.35 mm and 12.7 mm diameter spheres for cavitation numbers between 0.1 and 0.5. Also shown is the postion of laminar boundary layer separation upstream of the cavity detachment. The trends in the data for the sphere are similar. The position of cavity detachment is upstream of the location of non-cavitating laminar boundary layer separation.

The non-cavitating flow separation on the cylinder was examined. Figure 13 shows the angle of boundary layer separation measured from the front stagnation point of the cylinder. Dye visualization was used to locate separation. The trends are somewhat different, with the sphere having a much greater dependence on the Reynolds

Hydrofoil	Re_C	σ	Maximum thickness	Non-cavitating b.l. separation	Cavitating b.l. separation	Cavity detachment
NACA $\alpha = 0°$	1.1×10^6	0.35	35%	57%	37%	42%
Custom $\alpha = 1.5°$	8.9×10^5	0.39	36%	52%	29%	38%
Custom $\alpha = 3.0°$	8.9×10^5	0.44	36%	49%	28%	37%

TABLE 1. Position of the boundary layer separation and cavity detachment on the hydrofoils (% of chord measured from the leading edge).

number than the cylinder. The critical Reynolds number for turbulent boundary layer transition on a smooth sphere is approximately $Re_D \approx 2 \times 10^5$, and range of Reynolds numbers tested bracket this value. For the cylinder, however, the critical Reynolds number is approximately $Re_D \approx 3 \times 10^5$, which is greater than the largest Reynolds number investigated here. Therefore, the effects of natural boundary layer transition were not obseved in the cylinder data.

The free-stream pressure was reduced and air was injected into the wake of the cylinder, forming a fully developed ventilated cavity. As was seen on the sphere, the presence of an attached cavity affected the location of flow separation on the cylinder. Figure 14 shows the angle of boundary layer separation and cavity detachment versus Reynolds number for a narrow range of cavitation numbers. These data are for σ from 1.1 to 1.3. The cavitating flow separation remained relatively constant and the cavity detachment angle moved upstream with increasing Reynolds number on the brass cylinder. The locations of cavitating flow separation and cavity detachment are further upstream on the cylinder when compared to the sphere.

4.2. *Hydrofoils*

The non-cavitating flow separation on the two hydrofoils was determined using particle streak visualization. Flow separation occurred on the NACA 63_1A012 hydrofoil at 57% chord for $\alpha = 0°$ and $Re_C = 3.2 \times 10^6$, where the Reynolds number is based on the hydrofoil chord length. For the non-cavitating custom designed hydrofoil, the flow separated at a distance of 52% chord for $Re_C = 8.9 \times 10^5$ and $\alpha = 1.5°$, and at 49% chord for $Re_C = 8.9 \times 10^5$ and $\alpha = 3.0°$. For both hydrofoils, the non-cavitating flow separation is downstream of the maximum thickness point.

The free-stream pressure was reduced and a two-dimensional natural cavity formed near the midchord of the hydrofoils. The position of cavity detachment was consistently upstream of the position of non-cavitating boundary layer separation. Particle streak visualization was used to determine the location of boundary layer separation upstream of cavity detachment. Table 1 presents a summary of the data.

5. Near surface pressure distributions

Using planar PIV, the velocity of the flow around the test objects at one instant in time can be determined in one plane. From these data, the pressure coefficient, C_p can be determined near the surface of the sphere: $C_p = P - P_o / \frac{1}{2}\rho U_o{}^2$, where P is the local pressure, P_o is the free-stream static pressure, U_o is the free-stream velocity and ρ is the liquid density. The flow outside the thin boundary layer near the surface of the sphere may be considered as a potential flow. Thus, the Bernoulli equation can be used to determine the coefficient of pressure from the local velocity, $U(\boldsymbol{x})$, where $\boldsymbol{x}$ is a position vector locating a point in the potential flow: $C_p = 1 - (U(\boldsymbol{x})/U_o)^2$.

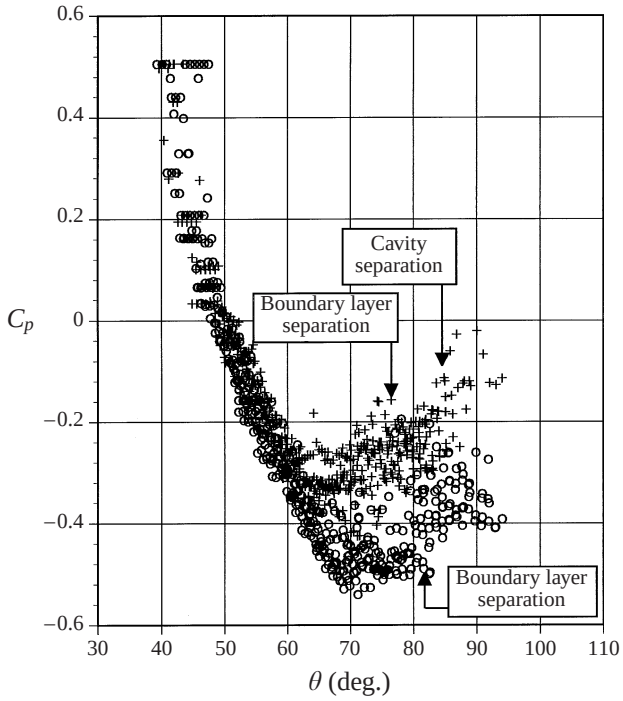

FIGURE 15. The pressure coefficient near the sphere surface for both non-cavitating (○) and cavitating (+) flows as a function of the angle from the stagnation point ($Re_D = 9.6 \times 10^4$). The data presented here are for six non-cavitating cases and six cavitating cases. The largest spread in the data is $\Delta C_p \pm 0.2$ which corresponds to a fluctuation in the velocity of $\pm 7\%$. The PIV uncertainty is approximately $\pm 6\%$ and the random error in the measurement of the freestream velocity is $\pm 2\%$. Marked on the figure is the location of the non-cavitating and cavitating flow separation angles and the cavity detachment angle.

An estimate was made of the boundary layer thickness based on the calculation of the fully wetted laminar flow, and velocity vectors were excluded which were within the estimated boundary layer. By examining the velocity vectors close to (but not in) the boundary layer of the sphere, the local pressure coefficient can be determined. Also, the transverse pressure gradient across the boundary layer is near zero, so the coefficient of pressure measured near the boundary layer approximates the coefficient of pressure on the surface of the sphere.

5.1. *Brass sphere and cylinder*

Figure 15 compares the pressure coefficient near the sphere surface for both non-cavitating and cavitating flows as a function of the angle from the stagnation point ($Re_D = 9.6 \times 10^4$). The data presented here are for six non-cavitating cases and six cavitating cases. Similarly, the pressure coefficient near the surface of the cylinder is shown in figure 16 ($Re_D = 1.2 \times 10^5$). The data presented represent six non-cavitating and eight cavitating data sets. The largest spread in the data is $\Delta C_p \pm 0.2$ which corresponds to a fluctuation in the velocity of $\pm 7\%$. The PIV uncertainty is approximately $\pm 6\%$ and the random error in the measurement of the free-stream velocity is $\pm 2\%$. Marked on the figure is the location of the non-cavitating and cavitating flow separation angles and the cavity detachment angle. From these data, it can be seen that the presence of the cavitation significantly changes the outer flow pressure field

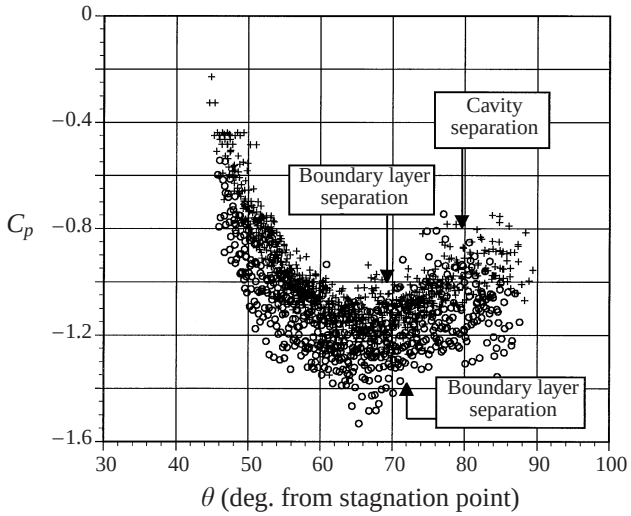

FIGURE 16. The pressure coefficient near the cylinder surface for both non-cavitating (○) and cavitating (+) flows as a function of the angle from the stagnation point ($Re_D = 1.2 \times 10^5$). The data presented represent six non-cavitating and eight cavitating data sets. The largest spread in the data is $\Delta C_p \pm 0.2$ which corresponds to a fluctuation in the velocity of $\pm 7\%$. The PIV uncertainty is approximately $\pm 6\%$ and the random error in the measurement of the freestream velocity is $\pm 2\%$. Marked on the figure is the location of the non-cavitating and cavitating flow separation angles and the cavity detachment angle.

before and after the cavity detachment point. Moreover, an adverse pressure gradient in observed upstream of the cavity detachment for both the brass sphere and cylinder.

5.2. *Hydrofoils*

Figures 17 to 19 present contours of pressure coefficient near the surface of the hydrofoils for the conditions presented in table 1. The coefficient of pressure is presented as a function of the distance from the stagnation point on the leading edge along the foil surface (not as a length along the chord). The data presented here are for five non-cavitating cases and five cavitating cases for each hydrofoil and attack angle. The scatter in the C_p data of magnitude ± 0.15 can be attributed to a $\pm 5\%$ uncertainty in the (independently measured) free-stream velocity. The uncertainty in the local velocities measured with PIV was approximately $\pm 7\%$. Marked on these graphs are the location of the non-cavitating and cavitating flow separation and the cavity detachment. The presence of the cavitation changes the pressure field in the entire region of the investigated flow. Also, a region of constant pressure near the cavity surface can be seen. There is an adverse pressure gradient upstream of the natural cavity, as was seen on the brass sphere and the brass cylinder for ventilated cavities.

6. Prediction of the location of flow separation

With the knowledge of the flow field near the non-cavitating and cavitating brass test objects, it was possible to predict the position of boundary layer separation which would produce a wake (in the non-cavitating case) or a cavity. The location of flow separation on the experimental test objects was calculated using the velocity distribu-

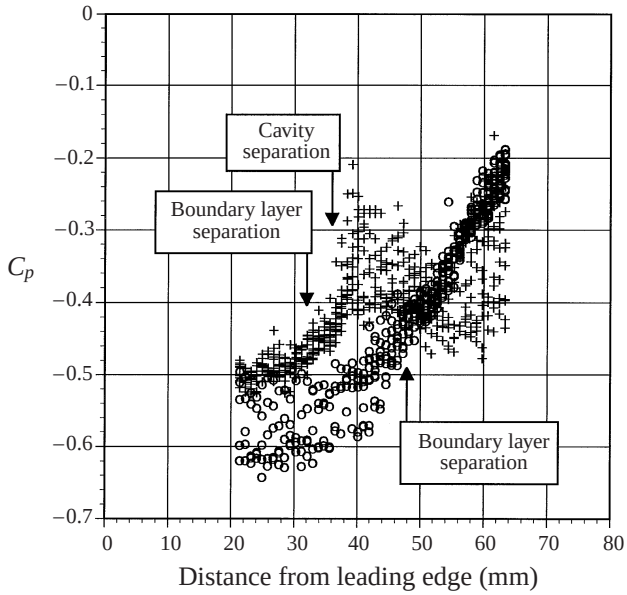

FIGURE 17. The pressure coefficient near the surface of the NACA 63_1A012 hydrofoil for the conditions presented in table 1. The coefficient of pressure is presented as a function of the distance from the stagnation point on the leading edge along the foil surface (not as a length along the chord). The data presented here are for five non-cavitating (○) and five cavitating (+) flows. The scatter in the C_p data of magnitude ± 0.15 can be attributed to a $\pm 5\%$ uncertainty in the (independently measured) free-stream velocity. The uncertainty in the local velocities measured with PIV was approximately $\pm 7\%$. Marked on the figure is the location of the non-cavitating and cavitating flow separation and the cavity detachment.

tions near the test object surface. Momentum integral techniques are commonly used to predict the location of two-dimensional flow separation.

Thwaites (1949) showed that the momentum thickness, θ_m, for all types of boundary layers can be predicted within $\pm 3\%$ using the following equation:

$$\theta_m{}^2 \approx \frac{0.45\nu}{U(x)^6} \int_0^\infty U(x)^5 \mathrm{d}x \tag{6.1}$$

where x is the distance measured along the surface from the upstream stagnation point. If $U(x)$ is known, the boundary layer parameter $\lambda = (\theta_m{}^2/\nu)(\mathrm{d}U/\mathrm{d}x)$ can be determined:

$$\lambda_{bl}{}^2 \approx \frac{0.45}{U(x)^6} \frac{\mathrm{d}U}{\mathrm{d}x} \int_0^\infty U(x)^5 \mathrm{d}x. \tag{6.2}$$

Thwaites observed that the boundary layer would separate when $\tau_w = 0$ which corresponds to a particular value of λ_{bl}. Curle & Skan (1957) determined that the best value of λ_{bl} at separation for all around accuracy was $\lambda_{bl,sep} = -0.09$. Thwaites' method can be combined with the Mangler transformation to produce a similar relationship for axisymmetric flows:

$$\lambda_{bl}{}^2 \approx \frac{0.45}{U(x)^6 r_o{}^2} \frac{\mathrm{d}U}{\mathrm{d}x} \int_0^\infty r_o{}^2 U(x)^5 \mathrm{d}x \tag{6.3}$$

where r_o is a function of x, the distance from the leading-edge stagnation point. The same separation condition exists for axisymmetric cases, namely, $\lambda_{bl,sep} = -0.09$.

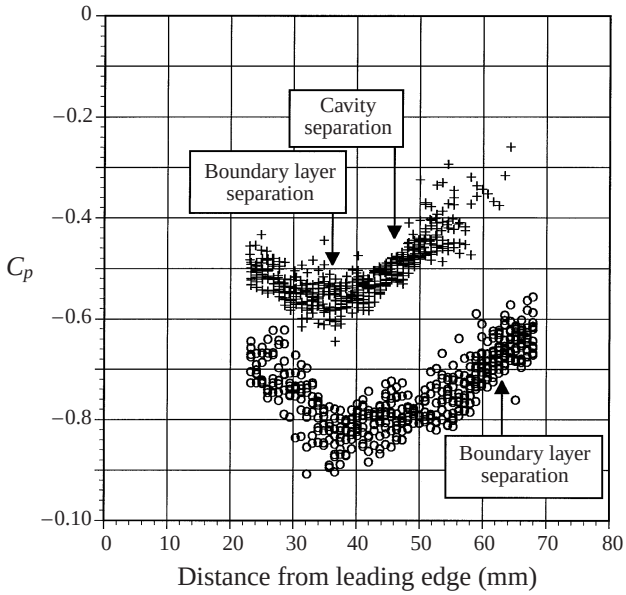

FIGURE 18. As figure 17 but for the Custom hydrofoil at $\alpha = 1.5°$.

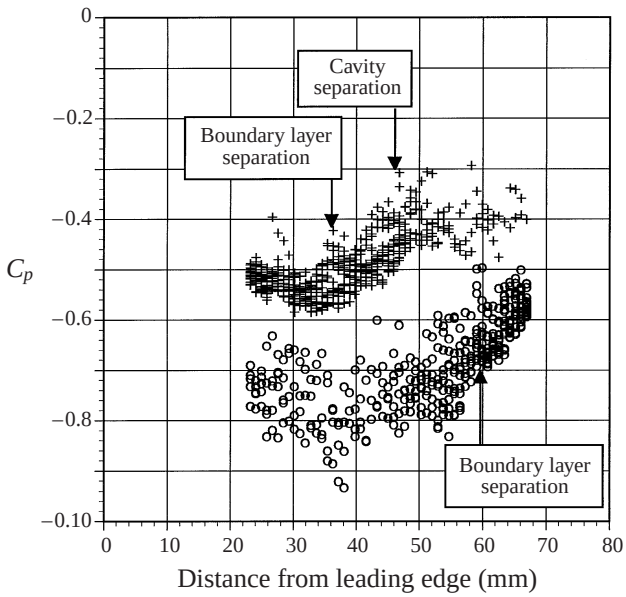

FIGURE 19. As figure 17 but for the Custom hydrofoil at $\alpha = 3.0°$.

Stratford (1954) constructed a different method to determine the location of laminar boundary layer separation. He divided the boundary layer into an outer layer and an inner layer. In the outer layer, he showed that the velocity profile could be predicted after considering the effect of the viscous forces and pressure forces separately. In the inner layer, a balance exists between the viscous and pressure forces. Pressure forces are balanced by viscous forces near the wall, but as one moves toward the edge of the boundary layer, the pressure forces are balanced by inertia forces. After matching

these inner and outer regions, and recognizing that $\tau_w = 0$ at separation, Stratford proposed a criterion for boundary layer separation:

$$(x - x_o)^2 \hat{C}_p \left(\frac{\mathrm{d}\hat{C}_p}{\mathrm{d}x} \right)^2 = \text{constant} \tag{6.4}$$

where

$$x_o = x_m - \int_0^{x_m} \left(\frac{U(x)}{U_m} \right)^5 \mathrm{d}x \tag{6.5}$$

and

$$\hat{C}_p = 1 - \left(\frac{U(x)}{U_m} \right)^2. \tag{6.6}$$

$\hat{C}_p$ is the normalized coefficient of pressure, U_m is the maximum velocity of the outer flow, and x_o is an artificial origin used to account for the momentum of the boundary layer which comes before the point of maximum velocity, x_m. Note that $\hat{C}_p$ is based upon the maximum velocity, U_m, not the free-stream velocity U_o. Thus, $\hat{C}_p$ will vary from zero to one. Curle & Skan (1957) determined the constant that most accurately predicted the separation for the majority of cases was ≈ 0.0104. Stratford's method has not been modified for axisymmetric flows.

Thwaites' method is a more general approach, since it tracks the momentum in the boundary layer throughout the calculation, in regions of both negative and positive pressure gradients. Stratford's method is local and applies to regions of positive pressure gradient. A correction for regions of negative pressure gradient is included with an artificial origin. Despite these differences, both methods are reasonably accurate and simple to apply.

6.1. *Brass sphere and cylinder*

A fifth-order odd-series polynomial equation was used to curve fit the velocity data from the PIV for the non-cavitating and cavitating flow near the surface of the brass sphere and cylinder. Such a polynomial was chosen because it corresponds to a Taylor series expansion of the inviscid flow solution. For the sphere, $U(x^*)/U_o = \frac{3}{2}\sin(x^*)$. For the cylinder, $U(x^*)/U_o = 2\sin(x^*)$. The distance along the surface from the stagnation point, x, is non-dimensionalized with the object radius, a ($x^* = x/a$). The fitted equations were forced through the point $U(x^*)/U_o = 0$ at $x/a = 0$, to enforce zero velocity at the stagnation point. Note that the value for U_o was acquired from the calibrated differential pressure measurement across the test section contraction and not from the PIV image. The curve fitted equations for the four cases are

non-cavitating sphere
$$\frac{U(x^*)}{U_o} = 0.994x^* + 0.218(x^*)^3 - 0.151(x^*)^5, \tag{6.7}$$

cavitating sphere
$$\frac{U(x^*)}{U_o} = 0.980x^* + 0.272(x^*)^3 - 0.201(x^*)^5, \tag{6.8}$$

non-cavitating cylinder
$$\frac{U(x^*)}{U_o} = 1.878x^* + 0.401(x^*)^3 - 0.029(x^*)^5, \tag{6.9}$$

cavitating cylinder
$$\frac{U(x^*)}{U_o} = 1.454x^* + 0.151(x^*)^3 - 0.219(x^*)^5. \tag{6.10}$$

Figures 20 and 21 present plots of the above functions with the associated experi-

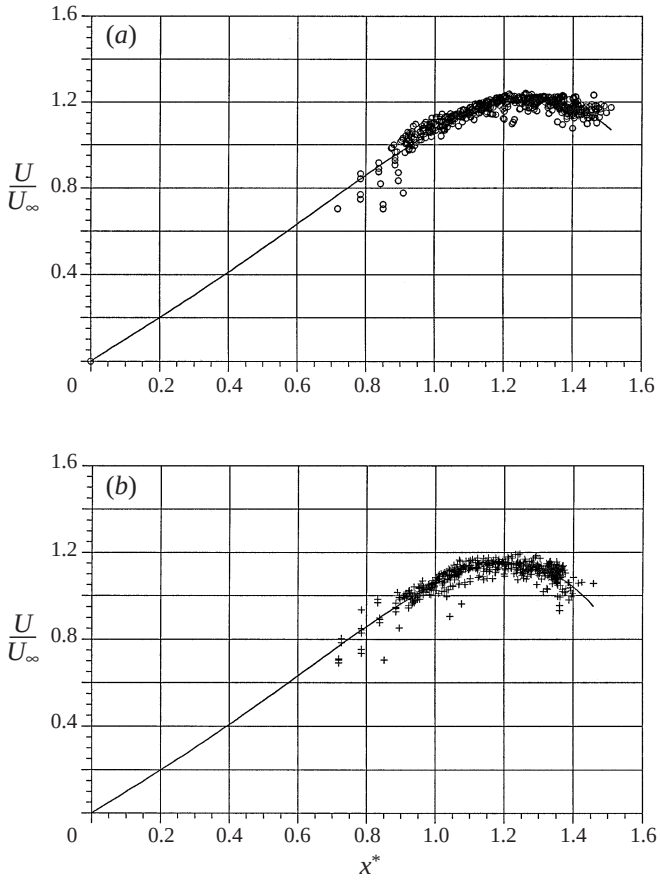

FIGURE 20. Flow speed near the surface of the sphere for the (*a*) non-cavitating and (*b*) cavitating flow. Also shown is a curve fit of the data (equations (6.7) and (6.8)).

mental data. These curve fits were then employed with Thwaites' method to predict the location of boundary layer separation for the cavitating and non-cavitating sphere and cylinder. Stratford's method was also used to predict the location of separation on the cylinder.

6.2. *Hydrofoils*

Unlike the flows around the sphere and cylinder, analytical solutions were not readily available for the flows around the two hydrofoils. However, prediction of the flow separation location with Thwaites' method required knowledge of the entire outer potential flow between the point of flow separation and the leading-edge stagnation point. The flow field data acquired through PIV included only a portion of this flow field for the non-cavitating cases. Thus, it was necessary to approximate the unknown portion of the flow field near the hydrofoil leading edge. A two-dimensional potential flow solution of the flow around the hydrofoils in the test section was generated to provide an approximate representation of the flow. PIV results for the cavitating flows were sufficient to predict the location of boundary layer separation.

The flow simulation package, RAMPANT, was used to simulate the two-dimensional potential flow around the hydrofoils. Foil and test section geometry was entered into the program GEOMESH and a mesh was generated. The inlet of the domain

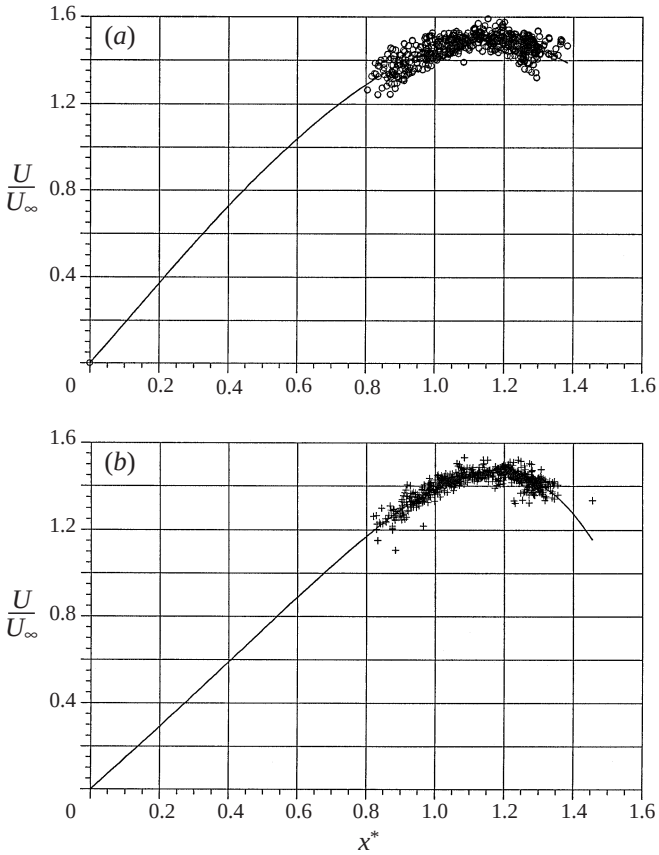

FIGURE 21. Flow speed near the surface of the cylinder for the (*a*) non-cavitating and (*b*) cavitating flow. Also shown is a curve fit of the data (equations (6.9) and (6.10)).

was approximately one chord length upstream of the foil leading edge and extends approximately one chord length downstream of the trailing edge. The walls of the test section were included. The triangular, unstructured mesh had 13244 nodes. This mesh was imported into RAMPANT. The inlet flow was uniform and set to 15 m s^{-1}. The fluid was water and a solution of the Euler equations was calculated on the grid. Once completed, the flow velocity near the surface of the foil was exported. A process of grid refinement was undertaken until computational limitations were experienced. Changes in the final grid produced changes in the surface velocity data on the order of $\pm 1\%$ in the region of interest. Similar calculations were performed for the custom hydrofoil at 9 m s^{-1} free-stream velocity and at 1.5° and 3° attack angle.

These calculated non-cavitating potential flows around the hydrofoils were used to approximate the flow at the leading edge. These data were matched to the PIV flow data near the region of flow separation for the non-cavitating flow. Unlike the case of the sphere and cylinder, the fluid velocity near the foil surface was scaled with the maximum velocity near the maximum thickness of the foil, not the free-stream velocity. This value was determined from the PIV images. Figures 22 to 24 show the cavitating and non-cavitating flow velocity near the surface of the hydrofoils measured with PIV, along with the non-cavitating potential flow solution. For the PIV data, the maximum velocity was measured from the PIV image, and for the potential

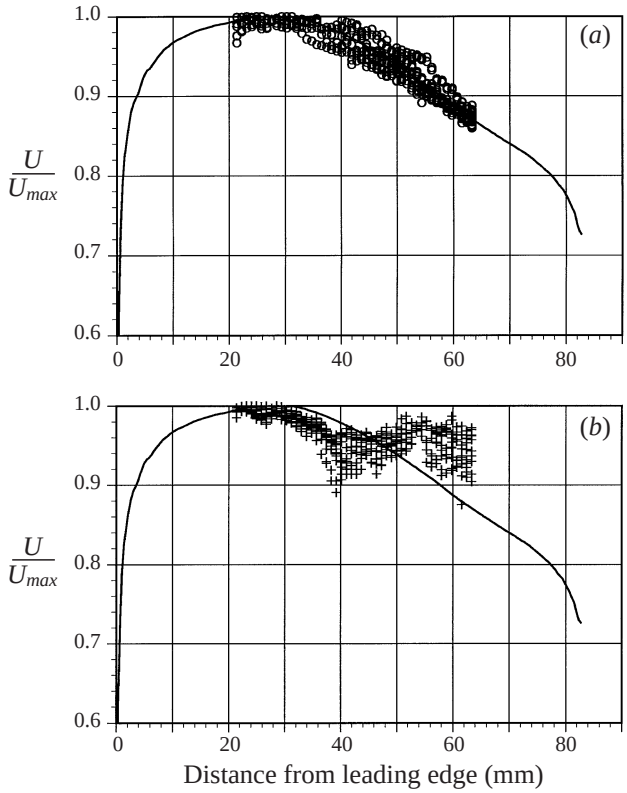

FIGURE 22. (*a*) The non-cavitating and (*b*) cavitating flow speed near the surface of the NACA 63_1A012 hydrofoil measured with PIV, along with the non-cavitating potential flow solution.

flow solution, the maximum velocity was taken from the calculation. For the NACA hydrofoil, the velocity distribution over the hydrofoil had only one maximum. The custom hydrofoil, however, had two local velocity maxima at both angles of attack: one near the leading edge and one near mid-chord. In order to compare with the PIV data, the potential flow solutions were scaled by the second maximum velocity near the centre of the hydrofoil (which was measured with PIV). Thwaites' and Statford's methods were then used to determine the location of non-cavitating and cavitating boundary layer separation.

6.3. *Comparison between predicted and observed location of boundary layer separation*

Table 2 summarizes the calculated and experimentally determined location of flow separation on the sphere, cylinder, and hydrofoils. Uncertainty in the predicted values from Thwaites' and Stratford's methods was at least $\pm 3\%$ but probably closer to $\pm 5\%$ for these cases. The uncertainty in the experimental measurement of boundary layer separation was conservatively estimated to be $\pm 5\%$. The predicted and measured position of boundary layer separation on the sphere, cylinder, and hydrofoils match within the limits of the uncertainties in the experiments and calculations.

The largest difference between the predicted and measured location of boundary layer separation was evident on the custom hydrofoil under cavitating conditions. Stratford's method resulted in the poorest prediction. This resulted from the inadequacies of the method. The custom hydrofoil exhibited two local minima in pressure

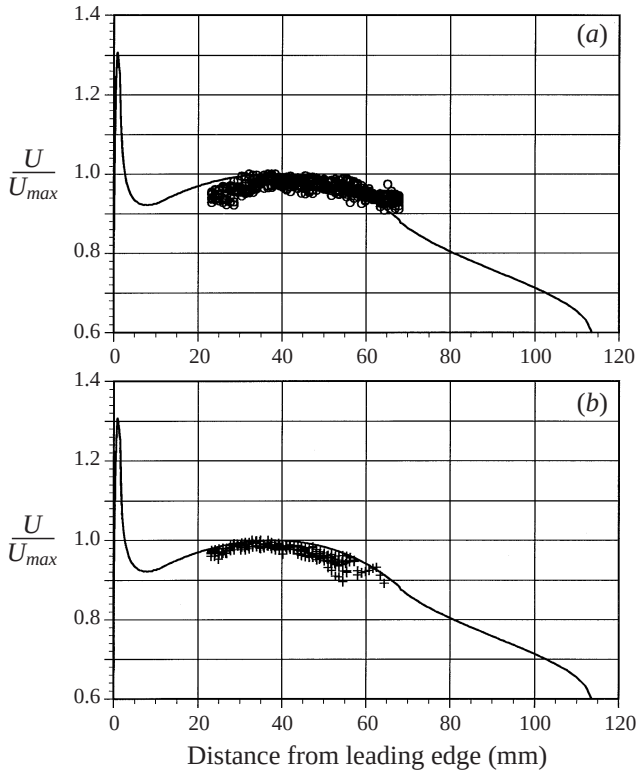

FIGURE 23. As figure 22 but for the Custom hydrofoil at $\alpha = 1.5°$.

upstream of the cavity separation. Thus, it is difficult to determine the artificial origin used to account for the regions of negative pressure gradient.

7. Conclusions

In the present work, the description of the separation region presented by Arakeri (1975) was observed on the hydrophilic (brass) test objects. Researchers have conjectured that recirculating liquid flow exists upstream of the cavity detachment, and this was observed for the brass (hydrophilic) test objects. The local cavity thickness near detachment, h, was on the order of the boundary layer thickness upstream of detachment. However, the measured interfacial curvature suggested that pressure differences across the interface resulting from liquid/vapour surface tension represent a small perturbation of the local liquid pressure. It is therefore expected that the local flow will be only weakly dependent on the Taylor–Saffman number. This was also suggested by Franc & Michel (1985) and Brennen (1995).

However, it was shown that changes in the liquid/solid work of adhesion significantly affected the flow near cavity detachment. On the brass (hydrophilic) test objects, the cavity interface curved downstream to form a forward facing step. A region of recirculating fluid was observed in the region bounded by the separation streamline and the cavity interface. The geometry of this step was related to the position of boundary layer separation upstream of the cavity. On the Teflon (hydrophobic) test objects, the cavity detachment was much closer to the location of boundary layer separation and the recirculating region was nearly absent. Also, the location of boundary

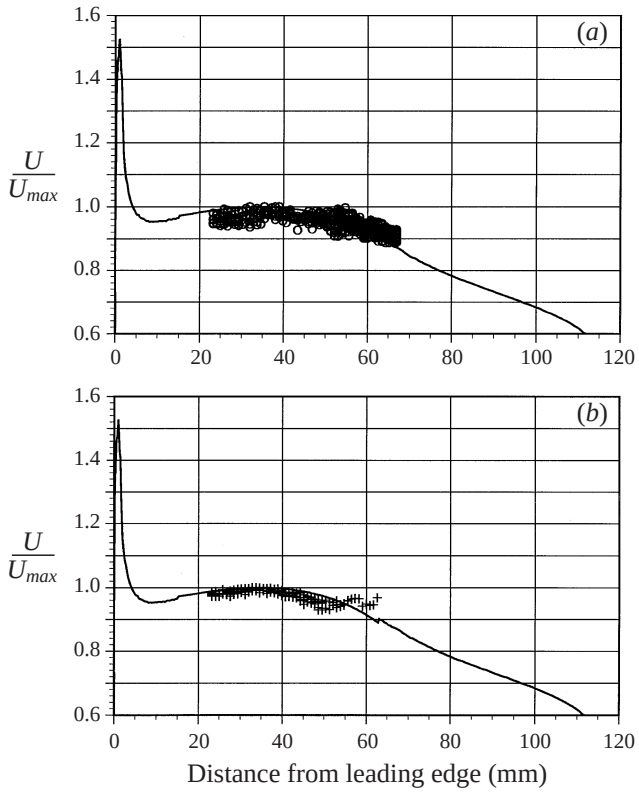

FIGURE 24. As figure 22 but for the Custom hydrofoil at $\alpha = 3.0°$.

layer separation was shifted a few degrees upstream on the hydrophobic object when compared to the hydrophilic object.

Both the liquid/gas interfacial tension and the solid/liquid work of adhesion determine the final interfacial geometry. Therefore, the Taylor–Saffman number (defined with the liquid/gas interfacial tension only) is not expected to completely scale the interfacial effects near cavity detachment. A parameter which includes the solid/liquid work of adhesion (such as ΔW) may yield better scaling results. Variation of the solid/liquid work of adhesion can lead to significant changes in the local cavity geometry. For hydrophilic solid/liquid combinations (which include most metal/water systems), $\Delta W \approx 0$ and is independent of γ_{lg}. Thus, it is expected that variation of γ_{lg} will not influence the physics of the cavity detachment on hydrophilic materials. This was observed by Brennen (1970) for the cavity flows over brass spheres. A reduction in the surface tension of water by more than 50% had 'no measurable effect' on the cavity flow. However, for hydrophobic solid/liquid systems, $\Delta W \approx 2\gamma_{lg}$, and strong variation in the surface tension may influence the flow near cavity separation.

Franc & Michel (1985) proposed a mechanism through which cavities formed and stabilized, which was represented in figure 3. The inception of the cavity occurs in a region of fully wetted laminar boundary layer separation. The cavity, in turn, modifies the entire flow field. If the new cavitating flow field leads to a laminar separation upstream of the cavity detachment, the cavity will be stable. This reasoning leads to the 'separation paradox'. A boundary layer separation upstream of the cavity implies that the cavity pressure is not the minimum pressure in the flow. However, for natural

Object	Condition	Thwaites' method	Stratford's method	Experimentally observed
Sphere	NC-PIV	$80 \pm 4°$	–	$82 \pm 4°$
	C-PIV	$75 \pm 4°$	–	$78 \pm 4°$
Cylinder	NC-PIV	$74 \pm 4°$	$75 \pm 4°$	$72 \pm 4°$
	C-PIV	$73 \pm 4°$	$74 \pm 4°$	$70 \pm 4°$
NACA hydrofoil	NC-PIV	$56 \pm 3\%$	$58 \pm 3\%$	$57 \pm 3\%$
$\alpha = 0°$	C-PIV	$36 \pm 2\%$	$38 \pm 2\%$	$42 \pm 2\%$
Custom hydrofoil	NC-PIV	$54 \pm 3\%$	$49 \pm 3\%$	$52 \pm 3\%$
$\alpha = 1.5°$	C-PIV	$29 \pm 2\%$	$35 \pm 2\%$	$29 \pm 2\%$
Custom hydrofoil	NC-PIV	$47 \pm 3\%$	$48 \pm 3\%$	$49 \pm 3\%$
$\alpha = 3°$	C-PIV	$27 \pm 2\%$	$31 \pm 2\%$	$28 \pm 2\%$

TABLE 2. Position of the boundary layer separation for non-cavitating (NC) and cavitating conditions (C). Calculations are based on the PIV data (PIV) and are compared with the experimentally observed position of boundary layer separation. The position of boundary layer separation is the angle measured from the stagnation point. The position of boundary layer separation on the hydrofoils is % of chord measured from the leading edge.

cavities this implies that the liquid pressure is below vapour pressure upstream of the cavity (e.g. the liquid is in tension). Observations of the flow field near the cavity detachment confirm this mechanism for two-dimensional cavity detachment. PIV data indicate that the cavitating flow differed significantly from the non-cavitating flow. As expected, the cavity results in a significant modification of the non-cavitating flow.

A laminar boundary layer separation was observed upstream of the cavity, and the position of the separation differed from that of the non-cavitating flow separation. Images of the cavity on the hydrophilic test objects suggest that the cavity presents a forward facing step to the liquid flow. Such a barrier would necessarily lead to local flow separation upstream of the cavity. However, the postion of flow separation upstream of cavities on the hydrophobic test objects was nearly identical to that of the hydrophilic test objects. Therefore, the local cavity geometry near deatchment has only a small influence on the ultimate postion of cavity detachment. The presence of an incipient cavity will change the potential outer flow and thus modify the pressure gradients upstream of the cavity. The viscous boundary layer flow upstream of the cavity will then be modified. If the adverse pressure gradient persists and boundary layer separation results, then a stable cavity will result. Therefore, the postion of cavity detachment is linked to the viscous boundary layer upstream of the cavity principally through the potential outer flow.

Observations of the flow field showed that an adverse pressure gradient existed upstream of the cavity detachment. This was true for both ventilated and natural cavities. As such, the 'separation paradox' is answered: a surface pressure minimum must exist upstream of a smooth cavity detachment, even if the liquid must be in tension. Moreover, a prediction of the laminar separation was possible based on the classic mechanism for two-dimensional boundary layer separation. The measured potential outer flow did yield a relatively accurate prediction of the boundary layer separation upstream of cavity detachment. The influence of the cavity was found only in the potential flow field. The local cavity geometry near cavity detachment only slightly influenced the final position of cavity detachment. Thwaites' and Strat-

ford's methods were used to predict the location of boundary layer separation. The predictions for the non-cavitating and cavitating cases were within the experimental accuracy of the experimentally determined location of boundary layer separation. Stratford's method resulted in the poorest prediction. The cavitating brass cylinder and sphere also showed good agreement. Therefore, these relatively simple methods may be employed to predict the location of two-dimensional cavity separation. A potential flow solution of the two-dimensionsl cavitating flow may be combined with momentum integral methods to iteratively determine the postion of boundary layer separation upstream of cavity detachment on smooth objects.

In conclusion, we have determined the following for two-dimensional cavity detachment:

(i) The geometry of the cavity near detachment is strongly influenced by the solid/liquid work of adhesion. Variation in the liquid/gas interfacial tension is not expected to significantly modify the flow near the cavity detachment or the cavity geometry for hydrophilic solid/liquid systems.

(ii) An adverse pressure gradient exists upstream of the cavity detachment. This was true for both ventilated and natural cavities. For the natural vapour cavities, the liquid was in tension upstream of the cavity detachment.

(iii) The position of cavity detachment is determined through the interaction of the cavity, the modified outer potential flow, and the viscous boundary layer upstream of the cavity detachment. The position of laminar boundary layer separation upstream of the cavity detachment is not significantly influenced by variation in the local cavity geometry near detachment.

The authors would like to acknowledge the substantial assistance of Daniel Wasserman, Noah Shirk, and Kathy Laberteaux for their assistance in the reduction of the data. This work was supported by the Office of Naval Research contract numbers N00014-93-1-0029 and N00014-96-1-0076 with Dr Edwin P. Rood as the contract monitor.

REFERENCES

Achenbach, E. 1972 Experiments on the flow past spheres at very high Reynolds numbers. *J. Fluid Mech.* **54**, 565–575.

Arakeri, V. H. 1975 Viscous effects on the position of cavitation separation from smooth bodies. *J. Fluid Mech.* **68**, 779–799.

Arakeri, V. H. & Acosta, A. J. 1973 Viscous effects in the inception of cavitation on axisymmetric bodies. *Trans. ASME*: *J. Fluids Engng* **95**, 519–527.

Arakeri, V. H. & Acosta, A. J. 1976 Cavitation inception observations on axisymmetric bodies at supercritical Reynolds numbers. *J. Ship Res.* **20**, 40–50.

Brennen, C. 1970 Some cavitation experiments with dilute polymer solutions. *J. Fluid Mech.* **44**, 51–63.

Brennen, C. 1995 *Cavitation and Bubble Dynamics*. Oxford University Press.

Brillouin, M. 1911 Les surfaces de glissement de Helmholtz et la résistance des fluids. *Ann. Chim Phys.* **23**, 145–230.

Curle, N. & Skan, S. W. 1957 Approximate methods for predicting separation properties of laminar boundary layers. *Aeronaut. Q.* **8**, 257–268.

Davies, J. T. & Rideal, E. K. 1961 *Interfacial Phenomena.* Academic Press.

Franc, J. P. & Michel, J. M. 1985 Attached cavitation and the boundary layer: experimental investigation and numerical treatment. *J. Fluid Mech.* **154**, 63–90.

Li, C.-Y. & Ceccio, S. L. 1996 Interaction of single travelling bubbles with the boundary layer and attached cavitation. *J. Fluid Mech.* **323**, 329–353.

Maxworthy, T. 1969 Experiments on the flow around a sphere at high Reynolds numbers. *Trans. ASME*: *J. Appl. Mech.* 598–607.

Stratford, B. S. 1954 Flow in the laminar boundary layer near separation. *Aeronautical Research Council of London*, R&M-3003.

Tassin, A. L., Li, C.-Y, Ceccio, S. L. & Bernal, L. P. 1995 Velocity field measurements of cavitating flows. *Exps. Fluids* **20**, 125–130.

Tassin Leger, A., Bernal, L. P. & Ceccio, S. L. 1998 Examination of the flow near the leading edge of attached cavitation. Part 2. Incipient breakdown of two-dimensional and axisymmetric cavities. *J. Fluid Mech.* **376**, 91–113.

Tassin Leger, A. 1996 Experimental examination of the flow near the leading edge on an attached cavity, Doctoral Thesis, University of Michigan.

Thwaites, B. 1949 Approximate calculation of the laminar boundary layer. *Aeronaut. Q.* **1**, 245–280.

Villat, H. 1914 Sur la validité des solutions de certains problémes d'hydrodynamique. *J. Math Pure Appl.* (6) **20**, 231–290.